



Paper

Cite this article: Schmidt LS, Hvidberg CS, Kim JR, Karlsson NB (2019). Non-linear flow modelling of a Martian Lobate Debris Apron. *Journal of Glaciology* **65**(254), 889–899. <https://doi.org/10.1017/jog.2019.54>

Received: 5 September 2018

Revised: 23 July 2019

Accepted: 24 July 2019

First published online: 30 September 2019

Keywords:

Extraterrestrial glaciology; glacier flow; glacier mass balance; glacier modelling; ice temperature

Author for correspondence:

Louise Steffensen Schmidt,
E-mail: lss7@hi.is

Non-linear flow modelling of a Martian Lobate Debris Apron

Louise Steffensen Schmidt¹ , Christine Schött Hvidberg², Jung Rack Kim³ and Nanna Bjørnholt Karlsson^{4,5}

¹Department of Earth Sciences, University of Iceland, Reykjavik, Iceland; ²Centre for Ice and Climate, Niels Bohr Institute, University of Copenhagen, Denmark; ³University of Seoul, Seoul, South Korea; ⁴Alfred-Wegener-Institut Helmholtz-Zentrum für Polar-und Meeresforschung, Bremerhaven, Germany and ⁵Geological Survey of Denmark and Greenland, Copenhagen, Denmark

Abstract

The Martian mid-latitudes contain numerous small water-ice deposits, collectively termed viscous flow features (VFFs). The shape and topography of the deposits contain information on their past flow history and formation process. In order to access this information, it is imperative to get information on their deformational properties. Here we use a high-resolution digital topography map and ice-penetrating radar data in combination with an inverse method to constrain the deformational properties of a lobate debris apron, a class of VFF, in the southern hemisphere of Mars. We find that while the creep parameter and accumulation rates are not well constrained in absolute values, their ratio is robust. We also find that the creep exponent is most likely $n \leq 3$.

Introduction

High-resolution images of the Martian surface have revealed several geological features in the 40–60° latitude bands that exhibit detailed patterns consistent with the deformation of a soft material (e.g. Squyres, 1979; Head and others, 2010). These features, referred to as viscous flow features (VFFs) (Souness and others, 2012), are often situated on the slopes of high-relief landscapes (Milliken and others, 2003). Visually, they share characteristics with terrestrial debris-covered glaciers or rock glaciers. VFFs are divided into several sub-types, including glacier-like forms (GLFs), lobate debris aprons (LDAs), concentric crater fills (CCFs) and lineated valley fills (LVFs) (e.g. Levy and others, 2014; Souness and others, 2012). A study by Levy and others (2014) mapped over 11000 VFFs in the mid-latitude bands, and more than 1300 GLFs have been identified by Souness and others (2012). Radar sounding measurements by the SHARAD (SHallow RADar, see Seu and others, 2007) instrument on the Mars Reconnaissance Orbiter has proven that LDA deposits mainly consist of water ice with less than 10% lithic content (Holt and others, 2008; Plaut and others, 2009), and the composition of other VFFs is likely to be similar.

It is commonly assumed that the VFFs formed during different climatic conditions, since ice is currently not stable at the surface in the mid-latitudes (Mellon and Jakosky, 1995). The VFFs have likely survived due to a thin debris cover which has protected them from sublimation (e.g. Fastook and others, 2014). The thickness of the debris cover of LDAs is likely between 1 m (Feldman, 2004) and 10 m (Holt and others, 2008), which is small relative to the ice deposit thickness. The Martian climate undergoes substantial changes on timescales of 10 s of kyrs due to fluctuations in orbital parameters, such as obliquity changes (Laskar and others, 2002). Studies suggest that GLF deposits are 0.5–10 Myrs (e.g. Garvin and others, 2006; Souness and others, 2012; Hubbard and others, 2014), while LVF and LDA deposits are likely much older, from tens to hundreds of Myrs old (e.g. Mangold, 2003; Baker and others, 2010; Berman and others, 2015). This is consistent with the hypothesis that during periods of high obliquity, water ice became unstable at the poles and migrated to the mid-latitudes, which led to the formation of VFFs (Head and others, 2003).

The shape and topography of VFFs contain information on their formation process and past flow history (e.g. Karlsson and others, 2015; Brough and others, 2016). Previous studies have used similar assumptions to infer surface mass-balance patterns and flow history of the north polar layered deposits (NPLD) (Winebrenner and others, 2008; Koutnik and others, 2009), but whether the NPLD has a flow history has been heavily debated (e.g. Byrne, 2009). For example, Karlsson and others (2011) showed that the internal stratigraphy of the deposit, derived from SHARAD observations, is inconsistent with an ice sheet that has undergone significant flow. However, it is expected that local topographic features, such as troughs, craters and scarps, may be shaped by ice flow. For example, Pathare and Paige (2005) found that the dominant mechanism controlling NPLD trough morphology may be flow of subsurface ice, while Sori and others (2016) found that scarps at the NPLD margins could experience significant viscous flow. In a similar study, Pathare and others (2005) found that the distribution and depth of craters on the south polar layered deposit is most likely controlled by viscous flow, although the effect of viscous flow may be smaller for craters on the NPLD.

In this study, we investigate the deformational properties of a well-surveyed LDA surrounding Euripus Mons in the southern hemisphere of Mars. We estimate the value of the creep

© The Author(s) 2019. This is an Open Access article, distributed under the terms of the Creative Commons Attribution licence (<http://creativecommons.org/licenses/by/4.0/>), which permits unrestricted re-use, distribution, and reproduction in any medium, provided the original work is properly cited.

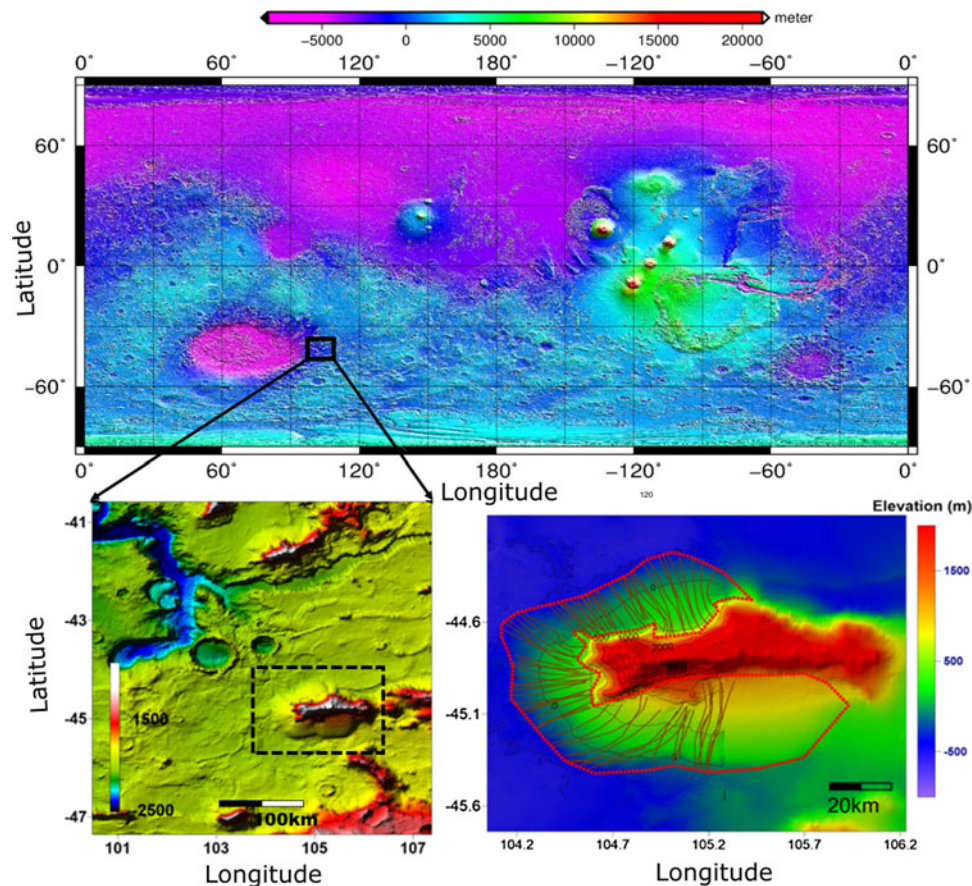


Fig. 1. Top: MOLA global topography with the location of the LDA marked with a rectangle. The elevation is relative to the areoid and the map uses a simple cylindrical projection. Bottom left: topography map of the area containing the LDA. The box shows the location of the bottom right figure. Bottom right: elevation of the LDA from MOLA (colours) and HRSC (black contours). The LDA is outlined with a dotted red line and used flowlines are marked with red solid lines.

exponent n as well as the accumulation rate and temperature regime. Our technique derives the basal topography below the ice deposit assuming steady-state accumulation rate along a 1-D flowline using a non-linear flow law for ice. We rely on a high-resolution digital elevation model (DEM) of the surface and a reconstructed bedrock created using SHARAD radar measurements and the topography of the surrounding area. The DEM was constructed from the High Resolution Stereo Camera (HRSC) (Gwinner and others, 2010) equipped on Mars Express and has a horizontal resolution of 70 m. This is a significant improvement compared with the MOLA DTM grid spacing (~150 m at our study site). In addition, Gwinner and others (2010) demonstrated that the vertical accuracy of the HRSC DEM achieved 11.2 m error level compared to MOLA once sophisticated sensor calibration and sub-pixel image matching are applied.

Study area and data

The selected study area is located at 105°E, 45°S (cf. Fig. 1). This area has several LDAs surrounding massifs, and on optical imagery the extents of the individual LDAs are clear. A high-resolution (70 m) HRSC DEM of part of the area, see Figure 2, was constructed by an effort employing an innovative photogrammetric adjustment procedure, i.e. sequential photogrammetric adjustment procedure and the densification of stereo intersection points as described in Gwinner and others (2010). It should be noted that the merits of HRSC DTM is not only in horizontal resolution but also its high-performance geodetic control which demonstrated 24 m height difference and 34 m standard deviation compared

with MOLA (Gwinner and others, 2010). The use of HRSC DTM should greatly reduce potential underestimation of local topographic slope of MOLA DTM, which can have up to a 30–40% error rate as proven in Kim and Muller (2009). The topographic slope underestimation by MOLA DTM was caused by two reasons according to the study by Kim and Muller (2009) employing Context Camera (CTX) and High Resolution Imaging Science Experiment (HIRISE) stereo DTMs; (1) the long sampling distances of MOLA observations especially in across track direction downgraded the vertical resolutions in the valuation model and occasionally skip locally populated steep surfaces in their measurements, (2) the big footprint size of MOLA spot which is 150 m and corresponding to several HRSC stereo measurements largely impaired the accuracy of vertical topographic measurements as stated in Gardner (1992). Thus the employment of HRSC DTM in our study was justified together with its proven geodetic control. This allows for the extraction of high-resolution measurements of the slope along estimated flow lines.

The area has been extensively surveyed by SHARAD, thus detailed information on the ice thickness can be reconstructed. The SHARAD dataset consists of 120 Reduced Data Records and was gathered using the Mars Orbital Data Explorer on the Planetary Data System Geosciences Node. The radar lines can be seen in Figure 2a.

Methods

Our methods rely on existing works on ice deformation. Experimentally, deformation of ice occurs due to several mechanisms that depend on temperature, stress and fabric, where each

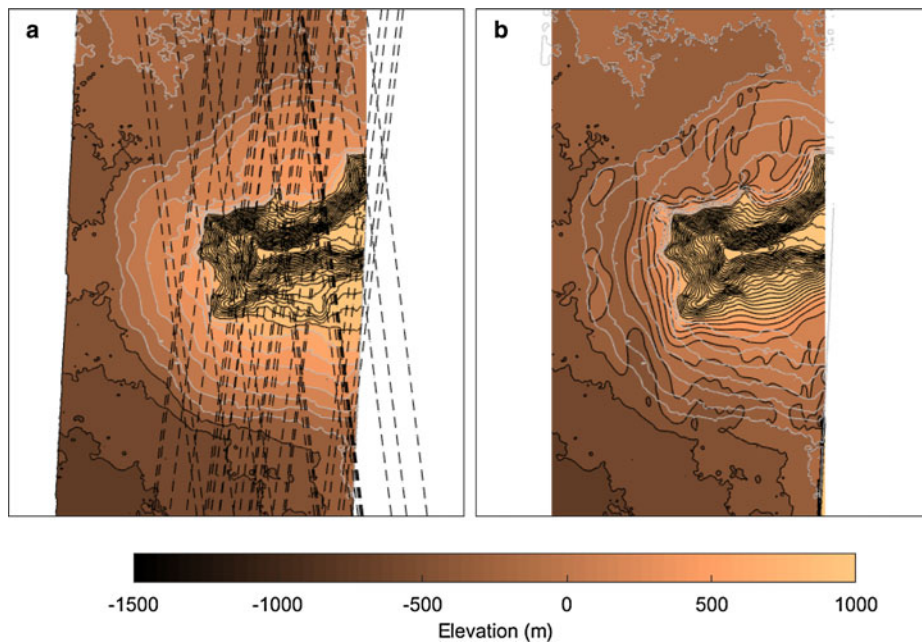


Fig. 2. (a) HRSC elevation map of the investigated area in colours and contoured in grey and black, with SHARAD lines in stippled black, and (b) the reconstructed bedrock topography where the grey contours correspond to the HRSC topography in (a).

mechanism has different values of the creep exponent n (e.g. Duval and others, 1983). In terrestrial glaciology, much work has gone into determining a single value of n which is appropriate for flow modelling of glaciers and ice sheets. This has been done through laboratory experiments (e.g. Glen, 1955; Goldsby and Kohlstedt, 2001) and field measurements (e.g. Paterson, 1977). The conventional value in terrestrial glaciology is $n=3$ (Cuffey and Paterson, 2010), but laboratory and field methods suggest values between 1 and 4, and an appropriate value of n is still being debated (e.g. Bons and others, 2018). Even if the features on Mars consist of pure water ice, different values of n may be needed to approximate the flow of Martian ice compared to ice on Earth. This is both due to Mars' lower gravity and the possible different shapes of Martian features, which means that the ice experiences different states of stress. Thus the relative importance of the different deformation mechanisms may differ from those of terrestrial glaciers.

Flow models of varying complexity have previously been successfully applied to Martian VFFs. For example, Fastook and others (2014) used a one-dimensional shallow-ice-flow model based on Glen's flow law (Glen, 1955) to study the formation of LDAs assuming they are remnant features of a regional ice mass. Parsons and Holt (2016) studied the build-up of an LDA by ice accumulation using a deformation law following Goldsby and Kohlstedt (2001). Here, we apply an approach similar to that of Karlsson and others (2015) where the ice deformation is modelled along flowlines using the shallow-ice approximation but we replace the plastic flow assumption with a non-linear model. Importantly, the validity of our method relies on the assumption of 'steady-state'. In terrestrial glaciology, this is the concept that the transport of mass due to ice deformation balances the mass input (e.g. accumulation) and mass output (e.g. calving), in other words, that the glacier or ice sheet is neither growing/advancing nor shrinking/retreating. Whether Martian water ice deposits are or have been in a steady-state is unknown. The formation of the VFFs likely took place during a different climate, and the transition to the present climate could have taken a number of Myr, during which time the shape of the LDA could have been modified past a steady-state shape. Whether the LDA is interacting with the atmosphere at present is also unknown, and in general, the interaction between ice reservoirs and the Martian atmosphere is still being debated. For example, experiments using Martian regolith simulants indicate that water

vapour discussion would produce a long-term average ice loss rate of less than 1 mm a^{-1} when buried below 1 m of regolith (e.g. Bryson and others, 2008). Given a lack of hydrogen detection on LDA surfaces by gamma-ray spectrometry (Feldman, 2004), the ice must be buried more than a metre deep. Although this is a slow rate compared to terrestrial standards, but as studies have suggested that sublimation from mid-latitude excess ice might still have taken place during the past 4 Myr (Bramson and others, 2017), the long duration may have resulted in a large amount of ice loss.

In spite of the mass loss from sublimation, some of the excess ice deposits in the subsurface are inferred to have been emplaced more than 10 million years ago (e.g. Viola and others, 2015), and modelling studies suggest that the interaction between atmosphere and ground ice was more active further back in time, while the present colder period has a comparatively low loss of ground ice (Grimm and others, 2017).

For our study, we must necessarily make the following assumptions:

1. the shape of the LDA is a steady-state shape.
2. the shape reflects that of a past climate and has not been modified substantially.

Our assumptions entail that the climate transition was short enough that the current shape of the LDA still reflects the past climate, and thus that the shape retains some information on past mass-balance and deformational properties.

To estimate the ice deformation of the LDA, we use that the surface velocity u_s can be determined by (Cuffey and Paterson, 2010)

$$u_s = \frac{2A}{n+1} \cdot \tau_b^n H, \quad (1)$$

where A is the ice softness, n is a flow exponent, τ_b is the basal shear stress and H is the ice thickness.

Construction of bed topography

In order to approximate the ice thickness of the LDA, a bed elevation map was constructed using the same method as Karlsson

and others (2015). First, the surface reflection and any subsurface reflections were picked manually on each radargram. We attempt to ensure that a subsurface reflection did not originate from off-nadir scattering by discarding any reflections that do not appear to be a natural continuation of the topography of the surrounding terrain. The thicknesses were retrieved by converting radar data from two-way travel time to elevation. This was achieved by matching the traced surface reflection to the high-resolution DEM topography and assuming that the deposits have the same dielectric constant as water ice (e.g. Holt and others, 2008; Grima and others, 2009). The measured two-way travel time t can thus be translated to ice thickness H using (e.g. Bogorodsky and others, 1985):

$$H = \frac{tc}{2\sqrt{k}}, \quad (2)$$

where k is the dielectric constant, assumed to be equal to that of water ice ($k=3.15$), and c is the speed of light in vacuum.

The SHARAD bed elevation measurements were then combined with data points from the ice-free terrain, in order to add as many constraints on the constructed bed as possible. We then used the Matlab function RegularizeData3D to calculate an interpolated bed topography. This function uses a set of irregularly spaced data points to create a smooth surface that best represents the data, while assuming a certain degree of smoothness of the surface. The resulting bed topography is shown in Figure 2.

Flow model

Ice is a semi-viscous material which deforms under an applied stress, where the rate of deformation depends non-linearly on the applied stress. Most models describing this deformation take the form

$$\dot{\epsilon} \propto \tau^f, \quad (3)$$

where $\dot{\epsilon}$ is the the shear strain rate, τ the shear stress and f depends on a number of factors, such as temperature and grain size, i.e. $f=f(T, d, \dots)$. For most terrestrial glaciers, this relationship is described by Glen's flow law (Glen, 1955):

$$\dot{\epsilon} = E\hat{A}\tau^n. \quad (4)$$

The creep exponent n is mostly assumed constant and equal to 3, although it can vary between 2 and 4 (e.g. Cuffey and Paterson, 2010; Gillet-Chaulet and others, 2011; Bons and others, 2018). Values of $n \approx 2$ typically occur at low stress while $n=4$ has been found to apply to high stresses (e.g. Goldsby and Kohlstedt, 2001). Its value depends on creep processes, crystal size, crystal fabric, effective stress, impurity content and liquid water fraction. The flow parameter \hat{A} depends strongly on the fabric and the temperature of the ice (Cuffey and Paterson, 2010). The additional E parameter is often included to account for softening of the ice due to, for example, anisotropy.

In planetary sciences, a similar relationship is often used in the form

$$\dot{\epsilon} = \tilde{A}\tau^n d^{-p} \quad (5)$$

from Goldsby and Kohlstedt (2001). Here, the additional term d is the ice crystal size and p depends on deformation mechanism. For low stress p takes values between 1 and 2.35 and $n=1.8$, while for high stress values $n=4$ and the crystal size dependency is negligible and thus $p=0$ (Goldsby and Kohlstedt, 2001).

We use the notation \hat{A} and \tilde{A} to distinguish between the two flow parameters that are not necessarily equal although they both take the Arrhenius form

$$A = A_0 \exp\left(-\frac{Q}{RT}\right), \quad (6)$$

where Q is the activation energy which may vary between 40 kJ mole^{-1} and 200 kJ mole^{-1} depending on the deformation mechanism and temperature (e.g. Weertman, 1983), T is the ice temperature and R is the gas constant. At times, the term Q is replaced by $Q+PV$, where Q is the activation energy for creep, P is the hydrostatic pressure, V is the activation volume for creep. A_0 is a constant whose value we discuss below and summarize in Table 1.

Regardless of whether we employ Eqn (4) or Eqn (5), we are faced with substantial uncertainties in terms of the values of either \hat{A} and E , or \tilde{A} and d . For example, the ice crystal size or orientation in the LDA is completely unknown and thus E and d are undetermined. It might be hypothesized that the crystal size is of the order of 10^{-4} m due to the possible inclusion of dust particles and other impurities, which have been observed to inhibit crystal growth in terrestrial ice sheets (e.g. Alley and Woods, 1996; Durand and others, 2006). In addition, the lower temperatures on Mars would likely also inhibit crystal growth (Kieffer, 1990). Previous studies have used values for d between 1 and 5 mm (Parsons and Holt, 2016). However, on Earth, deep ice-cores have been found to contain large ice crystals at depth, with, e.g. Eemian ice in Greenland having crystal sizes in the order of 25 mm (Dahl-Jensen and others, 2013). Since the ice crystals in the LDA have had unprecedented long time scales to grow, their size might be centimetre or even metre scale. We therefore consider the widest possible definition of ice deformation, i.e. that the shear strain rate depends non-linearly on the shear stress multiplied with some factor. We refer to this factor as A .

In order to further reduce the complexity of the problem, we only consider deformation of the ice along flowlines, thus reducing the problem to two dimensions. For this study we have used 77 flow lines. This is based on the assumption that ice flow occurs along the steepest surface gradient, which is a common assumption in terrestrial glaciology. The flowlines (see Fig. 1) were determined by starting at a number of points at the top of the LDA and following the surface gradient with a central-difference scheme (Budd and Warner, 1996). The flux balance along a flowline can then be expressed as (Cuffey and Paterson, 2010)

$$\dot{b}_i x = \frac{2A(\rho g)^n}{n+2} \left(-\frac{\partial S(x)}{\partial x}\right)^n H(x)^{2+n}, \quad (7)$$

where \dot{b}_i is the specific accumulation rate, $\rho = 918 \text{ kg m}^{-3}$ is the density of ice, $g = 3.71 \text{ m/s}^{-2}$ is the gravitational acceleration on Mars, $\partial S(x)/\partial x$ is the slope of the surface along the flow line, $H(x)$ is the ice thickness and x is the distance from the ice divide. Note that both the surface slope and the ice thickness vary along the flowline.

It is important to note that Eqn (7) is valid for ice masses with no sliding, uniform accumulation and a constant flowband width. Width of the flowlines used in this study are not calculated but are assumed constant. In addition, Eqn (7) assumes that ablation only occurs by calving at the edge, and the specific accumulation rate \dot{b}_i can therefore only assume positive values. We do not claim that Martian ice masses are calving, but instead assume that all ice ablation occur by sublimation at the toe of the LDA.

Table 1. Range of A_0 -values used in this study. The gas constant R is $8.314 \text{ J mol}^{-1} \text{ K}^{-1}$ and the volume creep activation energy V is $-1.3 \times 10^{-5} \text{ m}^3 \text{ mol}^{-1}$. Temperatures T range between -83 and -10°C

n	A_0 -value	d [m]	p	Q [J mol^{-1}]	A [$\text{Pa}^{-n} \text{s}^{-1}$]	Reference ^a
1 ^b	$3.9 \times 10^{-3} \text{ MPa}^{-n} \text{ m}^{-p} \text{ s}^{-1}$	$10^{-4} - 10^0$	1.4	66,000 ^c	$A = A_0 \cdot d^{-p} \cdot \exp(-(Q + PV)/(RT))$ $A_{n=1} = 2.8 \times 10^{-27}$ to 1.2×10^{-16}	GK-2001
2 ^b	$3.9 \times 10^{-3} \text{ MPa}^{-n} \text{ m}^{-p} \text{ s}^{-1}$	$10^{-4} - 10^0$	1.4	49000	$A = A_0 \cdot d^{-p} \cdot \exp(-(Q + PV)/(RT))$ $A_{n=2} = 1.3 \times 10^{-28}$ to 2.8×10^{-19}	GK-2001
3	$4.7 \times 10^{-13} \text{ Pa}^{-n} \text{ s}^{-1}$	N/A	N/A	60000	$A = A_0 \cdot \exp(-Q/(RT))$ $A_{n=3} = 9.2 \times 10^{-30}$ to 3.5×10^{-25}	CP-2011
4	$4.0 \times 10^{-19} \text{ Pa}^{-n} \text{ s}^{-1}$	N/A	N/A	60000	$A = A_0 \cdot \exp(-(Q + PV)/(RT))$ $A_{n=4} = 1.3 \times 10^{-35}$ to 4.8×10^{-31}	GK-2001

^aGK-2001: Goldsby and Kohlstedt (2001) and CP-2011: Cuffey and Paterson (2010).

^bPlease note we use the published A_0 -value for $n = 1.8$.

^c Q -value for $n = 1.6$ (Weertman, 1983).

Inverting for unknown model parameters

We use an inverse Monte Carlo scheme to infer the unknown model parameters, i.e. the accumulation rate b_i , the creep parameter A and the creep exponent n . Inverse methods use a data input with a pre-defined uncertainty to determine the unknown parameters of the system by exploring the model space to find the values that provide the best fits between model output and data. In this study, the data input is the interpolated bedrock created from SHARAD radargrams and the surface elevation from the HRSC data. The uncertainty of the data input was determined by interpolating our constructed bed to the location of the SHARAD radar lines and calculating the misfit. The misfit between radar lines and constructed bedrock was found to be 25%.

An inverse Monte Carlo scheme was run for five values of the creep exponent n . We use the same Monte Carlo scheme as published in Karlsson and others (2015), where a detailed description of the method may be found. Using this method, a range of realistic values of the unknown model parameters can be determined. In order to search the model space to determine the most likely value, constraints have to be put on each model parameter. In terrestrial studies, n generally ranges between 2 and 4 (e.g. Cuffey and Paterson, 2010; Gillet-Chaulet and others, 2011). In this study, we explore an interval between 1 and 5.

When allowing both the accumulation rate and creep parameter to vary, neither were well constrained. Instead, we inverted for the ratio between the two parameters (\dot{b}_i/A) and this approach produces robust results. Even so, we need a range of permitted values for both parameters to constrain the parameter space. Therefore, we assume that the LDA was formed during a climate where the temperature ranged between -83 and -10°C . This temperature range corresponds to a specific range in creep parameter value A depending on the choice of n (see Table 1). The accumulation rate, b_i is not well known either, but current atmospheric transport of water between the poles is smaller than 10^{-3} m a^{-1} (Byrne, 2009). Since we assume that the deposit was in balance with a previous climate, it is not unlikely that the shape of the LDA reflects a higher mass-balance regime. Several climate simulations show that the water cycle during obliquities above 35° is much more intense than at present (e.g. Richardson and Wilson, 2002; Forget and others, 2006). GCM studies have, for example, found accumulation rates on the order of $10^{-3} - 10^{-1} \text{ m a}^{-1}$, and the results by Madeleine and others (2009) show accumulation rates for the northern hemisphere between 1 and 16 mm. Forget and others (2006) finds the highest accumulation rate in Eastern Hellas on the southern hemisphere of 120 mm a^{-1} . As an upper limit for our inversion, the value of 120 mm a^{-1} was used. In a scenario where the precipitation was above 1 mm a^{-1} , the replenish age for the LDA would have been less than ~ 450 kyr. This is shorter than high-obliquity peaks during the last 5 Myrs, but much longer than similar

replenish ages of terrestrial glaciers, with, e.g. Icelandic glaciers having a replenish age of less than a few thousand years (e.g. Schmidt, 2019).

In the inverse Monte Carlo scheme, the model space was investigated using a random walk. During this walk, the Monte Carlo scheme randomly explores the parameter space within the predefined range for A/b_i . In our case, we did the inversion five times for the five different n -values. For each n -value, the simple flow model is run tens of thousands of times. Using a predefined probability function, the result from the flow model is either rejected or saved depending on the data-model misfit, resulting in a probability distribution of the most likely values of A/b_i . The random walk was continued until a stable probability distribution for each flow line was achieved. The ratio A/b_i was thus determined for each of the used flow lines.

Results

Using the average values of all the flowlines for \dot{b}_i/A in Eqn (7), we found that the flowlines have an average thickness of between 266 and 308 m, depending on the value of n . This is 17–59 m thicker than the mean thickness found from the SHARAD estimated bedrock (249 ± 50 m). The error is smallest for $n = 1$ and increases with increasing n -value (cf., Table 2). The reason for the overestimation of the thickness compared to the SHARAD estimation could be that more north-facing than south-facing flowlines have been used (45 north/north-west facing and 32 south/south-west facing), as generally, the thicknesses along flowlines on the south-facing LDAs are underestimated while those on the north-facing LDAs are overestimated (see Fig. 3). The possible reasons for this will be discussed in the next section. The results of the inversion are summarized in Table 2, and histograms of all the accepted values of the random walk can be seen in Figure 4. Since we did not invert for A directly, our results for the value of n apply to either choice of flow law (e.g. Eqn (4) or Eqn (5)).

Discussion

Error estimates

As shown in Table 2, the RMSE along the flowlines is in the range 87–113 m depending on the value of n . One of the reasons for the large errors is that there appears to be a difference in rheology between the north- and south-facing part of the LDA. The difference between the LDA thickness calculated using the mean value of \dot{b}_i/A and the thickness simulated from SHARAD has different signs for the south-facing and north-facing part of the LDA. This suggests that the south-facing part of the LDA (i.e. poleward-facing), where the thickness is generally underestimated, needs a higher \dot{b}_i/A ratio than the north-facing (i.e. equator-facing) part, where the thickness is generally overestimated, in order

Table 2. The mean values of the ratio between the accumulation rate and the creep parameter \bar{b}_i/A obtained from the inversion scheme, the root-mean square error (RMS) and the absolute percentage error ($-\epsilon_H$) of modelled ice thicknesses along flowlines compared to the radar estimated bedrock

n	area	\bar{b}_i/A [m Pa n]	RMSE [m]	$-\epsilon_H$ [%]	V [km 3]	ϵ_V [%]
1	All	2.5×10^5	86.6	30	435	-3.1
1	North	3.5×10^5	56.7	24	192	10.2
1	South	2.0×10^5	98.2	28	272	-0.4
2	All	7.4×10^9	90.8	32	441	-1.7
2	North	1.4×10^{10}	54.6	24	195	12.0
2	South	4.4×10^9	98.7	29	277	1.2
3	All	2.8×10^{14}	98.7	34	469	4.5
3	North	3.8×10^{14}	53.5	23	191	9.9
3	South	9.2×10^{13}	101.3	31	283	3.2
4	All	1.1×10^{19}	106.0	36	480	6.9
4	North	1.4×10^{19}	55.1	23	188	8.1
4	South	1.8×10^{18}	102.4	31	257	-6.2
5	All	4.9×10^{23}	113.3	37	504	12.2
5	North	5.4×10^{23}	61.0	26	200	14.8
5	South	6.9×10^{22}	104.0	32	257	-6.2

Volumes (V) are calculated using the interpolated modelled flowlines with the mean value of \bar{b}_i/A for each value of n , and the percentage error (ϵ_V) of the total volume compared to the SHARAD volume (~ 449 km 3) is given. The values calculated by using the whole area as well as by dividing the LDA into north and south facing parts are given.

to give the best fit. For example, the mean \bar{b}_i/A value for $n=3$ for only south-facing flowlines is 9.2×10^{13} m Pa $^{-3}$ (average slope $\sim 2^\circ$), whereas it is 3.8×10^{14} m Pa $^{-3}$ for north-facing flowlines (average slope $\sim 3^\circ$). The ratio for the south-facing flowlines is therefore 75% times higher than for the northern-facing ones. Using different \bar{b}_i/A values for the north- and south-facing

LDAs improves the uncertainties given in Table 2, especially for higher values of n . The absolute percentage error and the RMSE now lies between 27–31% and 80–86 m, respectively, depending on the value of n . The north-facing flowlines have an average RMSE of 53–61 m (23–26%) depending on n , while

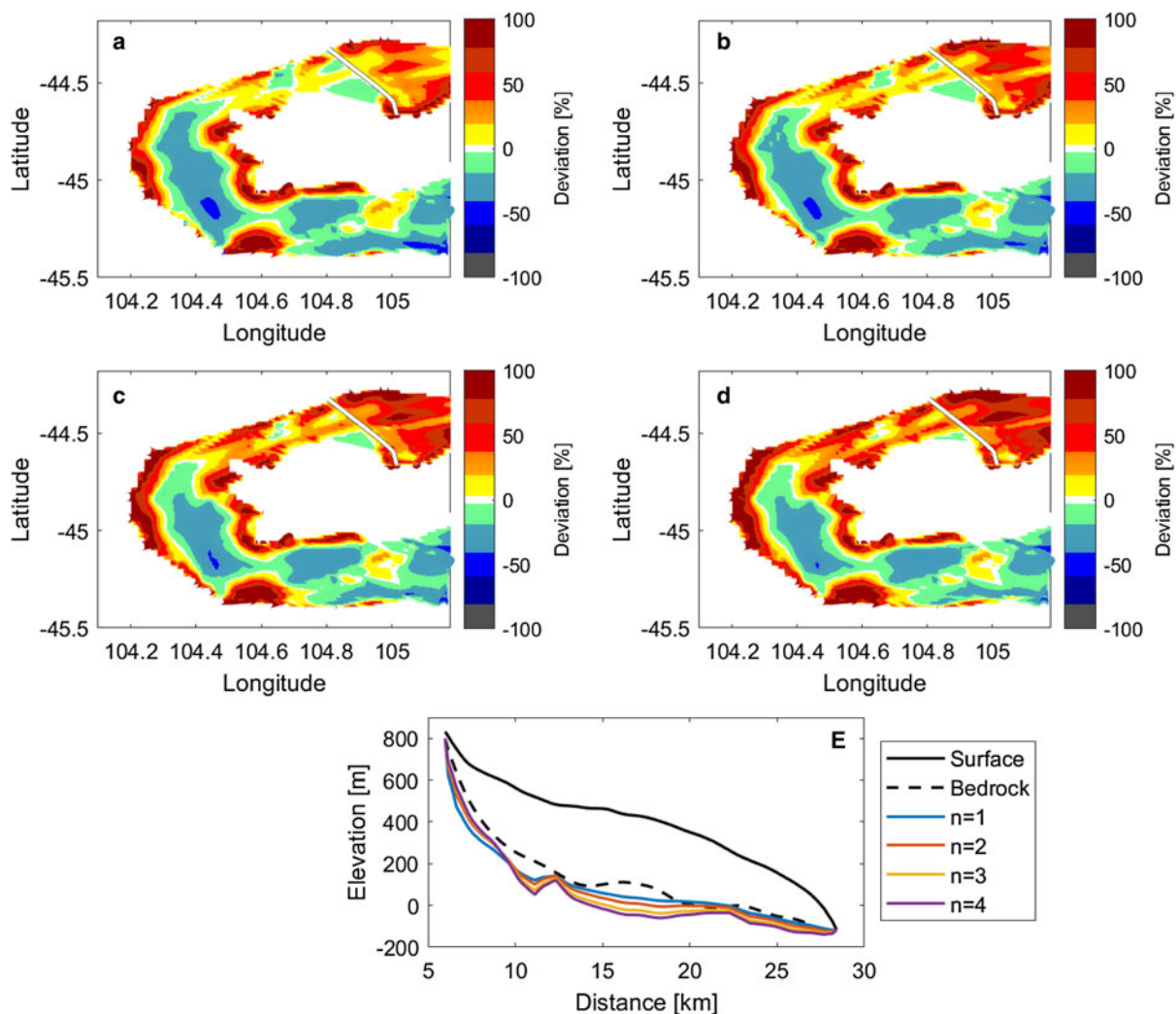


Fig. 3. (a)–(d) Percentage deviation between the SHARAD derived LDA thickness and the thickness found using modelled flowlines for (a) $n=1$, (b) $n=2$, (c) $n=3$ and (d) $n=4$. (e) Results along flowline (shown with white line in Figures a–d) for different values of n .

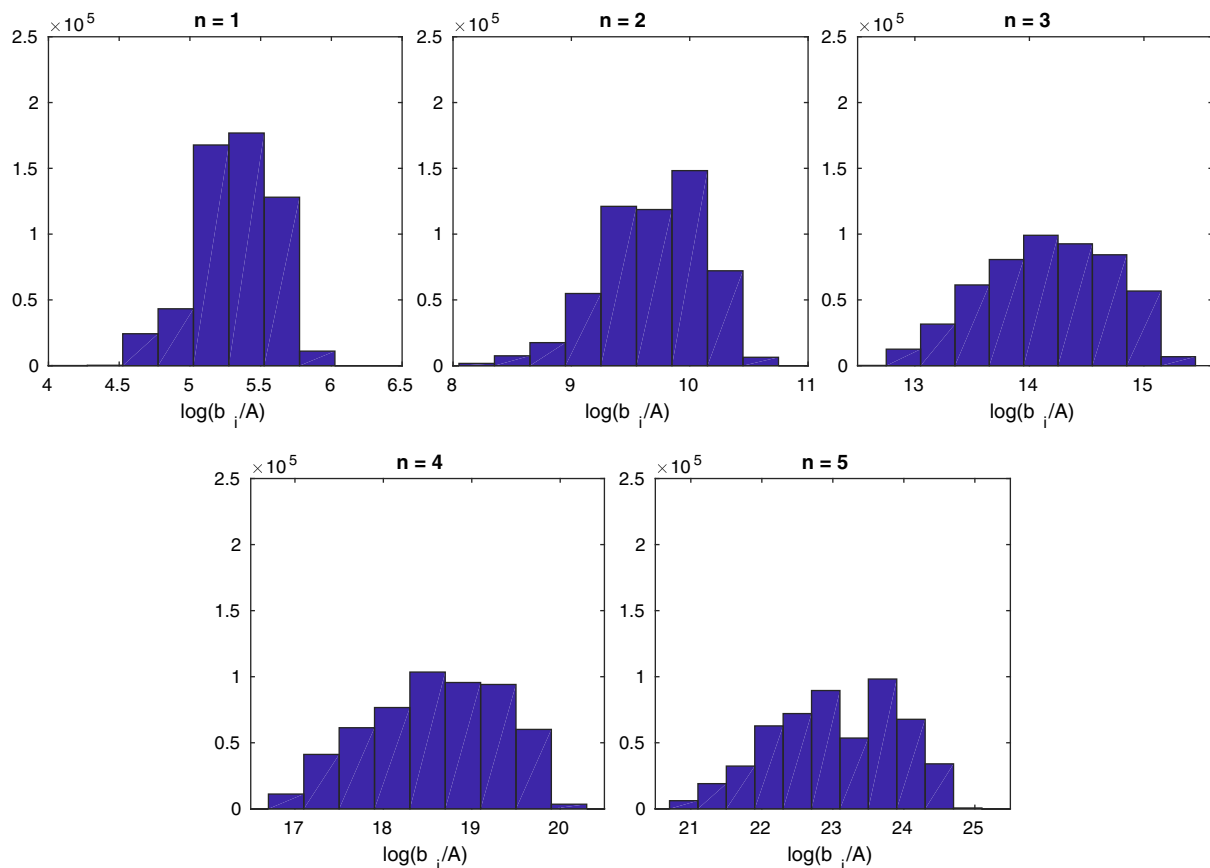


Fig. 4. Histograms of all accepted values of \dot{b}_i/A for each value of n in the random walk.

the south-facing flowlines have an average RMSE of 98–104 m (28–32%) (see Table 2).

Karlsson and others (2015) and Parsons and Holt (2016) also found that different parameterizations were needed for simulating the north- and south-facing parts of the LDA. Karlsson and others (2015) found differences in the yield stress between the north- and south-facing LDAs in this area, while Parsons and Holt (2016) found a difference in the rheological properties. Karlsson and others (2015) suggested that a possible explanation for this is that the two sides experience different mass-balance regimes, as the north-facing side receives more solar insolation and thus the ice may be warmer and softer and/or experience more sublimation. However, Parsons and Holt (2016) found that it is unlikely that only cause for the rheological differences is due to solar insolation, and instead suggested differences in ice grain size or timing of ice accumulation as potential explanations. Assuming that the formation of the VFFs was a global phenomenon, or at least took place on a large regional scale, this indicates that local processes and conditions may have impacted the formation or subsequently altered the shape of the LDA after it formed.

Parsons and Holt (2016) simulated the surface topography of the same LDA using a non-steady-state, time-marching simulation with $n=2$ and achieved an RMSE of 23–30 m (for bedrock slopes of 0.5–1.5°) for the north-facing part, which is a significantly better fit than achieved in this study. The model used in this study relies on a steady-state assumption and a constant mass balance which only ablates by calving at the edges, and using a more complex numerical, non-steady-state model therefore captures the shape of the LDA more accurately. However, they achieved RMSE of 86–115 m (for bedrock slopes of 1–2°) for the south-facing part, which is closer to the values found in this study.

Both Parsons and Holt (2016) and Karlsson and others (2015) simulated a more accurate profile of the entire LDA than was possible with the steady-state method used in this study. The reason for this is most likely that the assumption of a steady-state accumulation is a cause of error, as it neglects the time- and space-varying mass-balance history of the deposit.

Implications for accumulation rate and temperature

From the results presented above, we now have an estimate of the ratio \dot{b}_i/A for a range of different n -values. Here, we discuss how this ratio may be utilized to extract information on the accumulation rate and temperature assuming that our estimates from the inversion are correct. In the following, we use the mean \dot{b}_i/A for all flow lines to estimate the possible ranges of accumulation rate and temperature. In order to extract the absolute values of \dot{b}_i and A , we now have to make some assumptions on the value of A_0 , and, depending on which flow line we select, the values of d and p . Depending on the value of n we either apply the values for A from Glen's flow law ($n=3$) or from the reported values in Goldsby and Kohlstedt (2001). Table 1 gives an overview of the values we use and their reference.

The range of possible values for accumulation rate and temperature was found using the minimum and maximum allowed values of A and \dot{b}_i , and then solving the equations $\dot{b}_{i,\min} = A_{\min} \cdot (\dot{b}_i/A)_n$ and $\dot{b}_{i,\max} = A_{\max} \cdot (\dot{b}_i/A)_n$ for each value of n . For example, for $n=4$ the minimum accumulation rate was calculated as:

$$\dot{b}_{i,\min} = A_{\min,n=4} \cdot (\dot{b}_i/A)_{n=4} = 4.5 \times 10^{-9} \text{ m a}^{-1}. \quad (8)$$

This value is within the plausible accumulation range. We

Table 3. The estimated minimum and maximum values of \dot{b}_i and A for different values of n , found using the set minimum and maximum values for each parameter

n	max \dot{b}_i [m a^{-1}]	min \dot{b}_i [m a^{-1}]	max A [$\text{Pa}^{-n}\text{s}^{-1}$]	min A [$\text{Pa}^{-n}\text{s}^{-1}$]	max T [$^{\circ}\text{C}$]	min T [$^{\circ}\text{C}$]
1	2×10^{-9} – 9×10^{-4}	2×10^{-14} – 9×10^{-9}	3.0×10^{-22} – 1.2×10^{-16}	2.8×10^{-27} – 1.1×10^{-21}	–10	–83
2	2×10^{-7} – 7×10^{-2}	3×10^{-11} – 1×10^{-5}	7.2×10^{-25} – 2.8×10^{-19}	1.3×10^{-28} – 5.2×10^{-23}	–10	–83
3	3×10^{-3}	8×10^{-8}	3.5×10^{-25}	9.2×10^{-30}	–10	–83
4	2×10^{-4}	5×10^{-9}	4.8×10^{-31}	1.3×10^{-35}	–10	–83

A range in values is given for $n \leq 2$ to reflect the range in grain size (10^0 – 10^{-4} m).

Table 4. The estimated minimum and maximum values of the velocity u and viscosity η for different values of n , found using the set minimum and maximum values from Table 3

n	max u [m a^{-1}]	min u [m a^{-1}]	max η [Pa s]	min η [Pa s]
1	8×10^{-8} – 3×10^{-2}	7×10^{-13} – 3×10^{-7}	5×10^{20} – 2×10^{26}	6×10^{15} – 2×10^{21}
2	5×10^{-6} – 2×10^0	8×10^{-10} – 3×10^{-4}	3×10^{17} – 1×10^{23}	5×10^{13} – 2×10^{19}
3	6×10^{-2}	2×10^{-6}	4×10^{19}	1×10^{15}
4	3×10^{-3}	7×10^{-8}	7×10^{20}	2×10^{16}

A range in values is given for $n \leq 2$ to reflect the range in grain size (10^0 – 10^{-4} m).

therefore further conclude that the value of A_{min} in Eqn (8) is also possible. This value corresponds to a temperature of -83°C . The results for all values of n are summarized in Table 3.

The temperature range cannot be constrained for any of the values of n , as the calculated value of \dot{b}_i/A in combination with the chosen constraints on the accumulation rate allows for the whole range of A -values (Table 1). The maximum accumulation rate needed to obtain the current shape assuming steady-state conditions is found to be in the order of 10^{-2} – 10^{-9} m a^{-1} . In the likely scenario that the LDA was created during a previous climate with accumulation rates of the order of 1 mm a^{-1} or higher, our results indicate that the creep exponent should be $n \leq 3$. However, it should be noted that the values of A and \dot{b}_i are very dependent on grain size for $n \leq 2$. Larger grain size leads to lower values of A and the calculated value of \dot{b}_i lowers with the same factor. Thus, if we restrict the results to grain sizes of the order of 10^{-3} m (cf., Parsons and Holt, 2016), the values for the maximum accumulation rate are within the range of those estimated by Madeleine and others (2009).

Estimates of the velocities using Eqn (1) are given in Table 4. Unrealistically high velocities are found for $n = 2$ and a grain size of 10^{-4} m, but in general velocities of less than 1 mm a^{-1} are found. The velocity calculations therefore cannot help much in narrowing down the temperature range. When $n = 2$ and $d = 10^{-4}$, the calculated velocities lead to a horizontal movement of $\sim 2.4 \text{ km}$ over 10 Myr for a temperature of $T = 70^{\circ}\text{C}$. For all other cases, the horizontal movement is simulated to be between 0.05 and 190 m in 10 Myr for a temperature of $T = 70^{\circ}\text{C}$.

Flow properties

Goldsby and Kohlstedt (2001) provided evidence of four stress-dependent deformation mechanisms based on the laboratory experiments on fine-grained ice: (1) dislocation creep (at high stress regimes, $n = 4$), (2) superplastic flow (stresses below 100 kPa , $n = 1.8$), (3) basal slip ($n = 2.4$) and (4) diffusional flow (very low stresses, $n = 1$). The fact that $n = 3$ is suitable for a wide range of glaciers on Earth could be due to the combined effect of dislocation creep ($n = 4$) and superplastic deformation ($n = 1.8$) (Peltier and others, 2000).

For our study area, we hypothesize $n \leq 3$, based on the increasing errors for higher values of n . Furthermore, Karlsson and others (2015) estimated the yield stress of glaciers in this area to be only 37.7 kPa , which is consistent with the very low stresses

associated with diffusive deformation found by Goldsby and Kohlstedt (2001). If $n = 1$, this would indicate that the LDA is dominated by diffusional flow. Interestingly, in their experiments Goldsby and Kohlstedt (2001) found no evidence for diffusional flow even for very small grain sizes of 3 – 5×10^{-6} m. However, since Goldsby and Kohlstedt (2001) used much higher stresses (minimum of $\sim 2 \text{ MPa}$) than those experienced by Martian ice masses, diffusional flow on Mars could occur at larger grain sizes than 10^{-6} m. If $n = 2$, this indicates that the ice deformation is dominated by superplastic flow, probably in combination with other mechanisms. If $n = 3$, the deformation could be the combined effect of dislocation creep and superplastic deformation, similar to terrestrial glaciers. However, as the evolution of the crystal structure of ice that is several million years old is unknown, it is an open question how the ice crystals change over long time-scales to accommodate stress.

Qi and others (2018) found that if ice masses consist of $> 6\%$ of non-ice material, grain boundary sliding is impeded and the ice deforms only due to dislocation creep. A value of $n \leq 3$ is therefore consistent with an LDA consisting of $> 94\%$ ice.

Impact on volume calculations

We used the mean values of \dot{b}_i/A for five values of n to estimate the ice volume in the area. The LDA has a total area of $\sim 1970 \text{ km}^2$, and an estimated ice volume of 435 – 504 km^3 (Table 2), depending on the value of n . The LDA therefore has a mean thickness of 221 – 256 m . This is consistent with the results by Karlsson and others (2015), who found a mean thickness of $232 \pm 65 \text{ m}$ in the same area, although that study included the average thickness of several LDAs in their final estimate. The fact that our inversion indicates that $n = 1$ gives a reasonable result indicates that the method of Karlsson and others (2015) who estimated ice volumes using a simple plastic model is a good approximation. Estimating the volume using the bedrock estimated from SHARAD data leads to a total volume of $449 \pm 90 \text{ km}^3$ and a mean thickness of $228 \pm 46 \text{ m}$. We note that the modelled volume results are therefore within the 25% uncertainty of the estimated volume from the SHARAD bedrock.

Applicability to other deformational features

Caution should be exercised when transferring our results to other VFFs or indeed other deformational features on Mars.

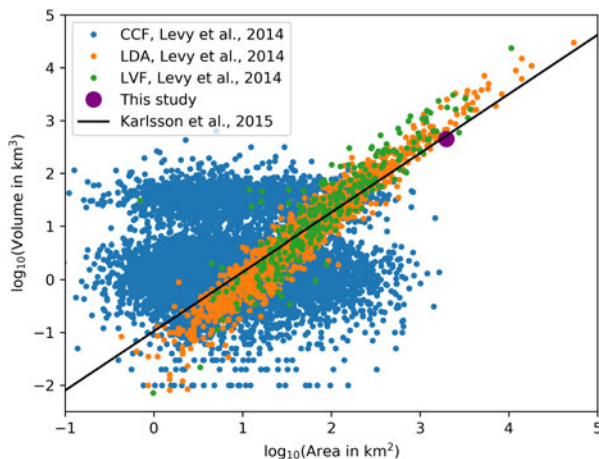


Fig. 5. The relationship between area and volume for VFFs mapped by Levy and others (2014). CCF, concentric crater fill; LVF, lineated valley fill; LDA, lobate debris apron. The relationship found by Karlsson and others (2015) is included as a black line.

For our results to be applicable, the composition of a feature should be predominantly water ice (H_2O) since large quantities of impurities ($> 10\%$) or the existence of other ices such as CO_2 might modify the deformational properties (cf., Parsons and Holt, 2016). Assuming that majority of VFFs are composed of H_2O -ice, we hypothesize that our results can be transferred to most LDAs and LVFs. This hypothesis is partly based on the wide range of model parameters permitted by the model results (see Table 3), which means that a large range of different temperatures and mass-balance regimes could be possible, and the results may describe a wide range of different LDAs. In addition, the hypothesis is based on the following observation: Using the dataset produced by Levy and others (2014), we plot all the CCFs, LDAs and LVFs mapped in the study on a $\log A$, $\log V$ -scale (Fig. 5). From the figure it is evident that the \log - \log relationship between area and volume is linear for the LDAs and LVFs. This is a strong indication that they share deformational properties and that those properties are likely similar to terrestrial glaciers and ice sheets as noted in Karlsson and others (2015). We therefore suggest that as long as the volume–area relationship for an LDA or LVF falls within the linear trend indicated in Figure 5, the deformational properties are likely to be similar to those of the LDA investigated here. However, it is important to note that this study still allows for large uncertainties in the ice rheology and accumulation rate, which means there are still large uncertainties in the deformational properties of these other LDAs.

It is interesting that the CCFs clearly do not follow a linear trend, which could indicate a different formation history, different water–ice content and/or a different mass exchange with the atmosphere. For example, Weitz and others (2018) suggest that CCFs started as lobate flow features which formed on crater walls, but with time the ice flowed into the crater floor. The shape of CCFs are therefore likely further from a steady state than LDAs.

In a broader perspective, our results indicate that care should be taken when transferring terrestrial deformation laws to extra-terrestrial water–ice. The viscous deformation of water–ice on, for example, Ceres, Europa, Enceladus, does not necessarily follow Glen's flow law (e.g. Miyamoto and others, 2005; Sori and others, 2017).

Conclusion

We investigate an LDA surrounding a massif in the southern hemisphere of Mars using SHARAD radargrams, a high-

resolution DEM and a non-linear 1D ice-flow model. We assume that the shape of the LDA is a steady-state shape and that it has not been modified since its formation. We apply an inverse Monte Carlo method in order to infer the unknown parameters in the model: the creep exponent n , the flow parameter A and the specific accumulation rate \dot{b}_i . In order to arrive at stable distributions, we invert for the ratio \dot{b}_i/A for four different values of the creep exponent; $n = 1, 2, 3, 4$ and 5 . Generally, the misfit between observations and model results increase with increasing values of n , with lowest absolute error for $n = 1$ (30%) and the highest absolute error for $n = 5$ (37%).

We further determine an interval of possible values of \dot{b}_i and A for values of $n = 1, 2, 3$ and 4 , using the mean value of the \dot{b}_i/A ratio. For the solutions where $n \leq 2$, the possible values depend on the grain size, and thus a large span in \dot{b}_i and A values is possible. In addition, a wide range of temperatures return a reasonable fit to the shapes. Therefore, while we cannot constrain the temperature, we infer that the values of $n \leq 2$ with a large grain size are most likely if the LDA shape was formed by a climate where little mass is exchanged between the atmosphere and the deposits, while if the grain size of the deposit is small ($\sim 10^{-4}$ m), a warmer climate with an accumulation rate in the order of 10^{-3} – 10^{-2} m a^{-1} is more likely. However, for $n = 2$ and a grain size $\sim 10^{-4}$ m, unrealistically high surface velocities are found. In the case of $n = 3$, a wide range of temperatures and accumulation rates can fit the shape of the flow lines. Thus, in this case we cannot exclude neither a cold, dry climate nor a warmer climate with the accumulation rates of the order of 10^{-3} m a^{-1} . We find similar results for $n = 4$, albeit with a maximum accumulation rates in the order of 10^{-4} m a^{-1} . However, since we obtain a better fit between observations and model results for $n \leq 3$ than for results for $n \geq 4$ we favour the scenarios where the likely value of n is $n \leq 3$. This also agrees with the studies suggesting that the LDA is most likely experiencing low stresses (Karlsson and others, 2015).

Using the mean values of the probability distributions, the ice depth along flowlines and the ice volume of the LDA is estimated. We find a total ice volume of 435–504 km^3 and a mean thickness of 221–256 m. This is consistent with the volume found using SHARAD data, which is 449 ± 90 km^3 . Finally, we conclude that a simple plastic model is a reasonable approximation to estimate ice volumes of LDAs.

Acknowledgments. LSS is supported by the University of Iceland Eimskip Fund. The Centre for Ice and Climate is funded by the Danish National Research Foundation. We gratefully acknowledge Isaac Smith, Michael Sori and an anonymous reviewer whose insightful comments and suggestions improved the quality of this manuscript. The data and results from this study can be obtained by contacting the corresponding author. HRSC products are freely accessible via Planetary Science Archive (PSA) of European Space Agency or Planetary Data System (PDS) of NASA.

References

- Alley RB and Woods GA (1996) Impurity influence on normal grain growth in the GISP2 ice core, Greenland. *Journal of Glaciology* 42(41), 255–260. doi: 10.3189/S0022143000004111.
- Baker DM, Head JW and Marchant DR (2010) Flow patterns of lobate debris aprons and lineated valley fill north of Ismeniae Fossae, Mars: evidence for extensive mid-latitude glaciation in the Late Amazonian. *Icarus* 207(1), 186–209. doi: 10.1016/J.ICARUS.2009.11.017.
- Berman DC, Crown DA and Joseph EC (2015) Formation and mantling ages of lobate debris aprons on Mars: insights from categorized crater counts. *Planetary and Space Science* 111, 83–99. doi: 10.1016/J.PSS.2015.03.013.
- Bogorodsky VV, Bentley CR and Gudmandsen PE (1985) *Electromagnetic Wave Propagation in Ice*. In *Radioglaciology*. Cambridge, UK: Cambridge University Press, pp. 32–47. doi: 10.1007/97894009527513.
- Bons PD and 6 others (2018) Greenland ice sheet: higher nonlinearity of ice flow significantly reduces estimated basal motion. *Geophysical Research Letters* 45(13), 6542–6548. doi: 10.1029/2018GL078356.

- Bramson AM, Byrne S and Bapst J** (2017) Preservation of midlatitude ice sheets on Mars. *Journal of Geophysical Research Planets* **122**(11), 2250–2266. doi: [10.1002/2017JE005357](https://doi.org/10.1002/2017JE005357).
- Brough S, Hubbard B and Hubbard A** (2016) Former extent of glacier-like forms on Mars. *Icarus* **274**, 37–49. doi: [10.1016/j.icarus.2016.03.006](https://doi.org/10.1016/j.icarus.2016.03.006)
- Bryson K, Chevrier V, Sears D and Ulrich R** (2008) Stability of ice on Mars and the water vapor diurnal cycle: experimental study of the sublimation of ice through a fine-grained basaltic regolith. *Icarus* **196**, 446–458. doi: [10.1016/j.icarus.2008.02.011](https://doi.org/10.1016/j.icarus.2008.02.011).
- Budd WF and Warner RC** (1996) A computer scheme for rapid calculations of balance-flux distributions. *Annals of Glaciology* **23**, 21–27. doi: [10.3189/S0260305500013215](https://doi.org/10.3189/S0260305500013215).
- Byrne S** (2009) The polar deposits of Mars. *Annual Review of Earth and Planetary Sciences* **37**(1), 535–560. doi: [10.1146/annurev.earth.031208.100101](https://doi.org/10.1146/annurev.earth.031208.100101).
- Cuffey K and Paterson W** (2010) *The Physics of Glaciers*. Cambridge, Massachusetts, US: Academic Press. doi: [10.1016/0016-7185\(71\)90086-8](https://doi.org/10.1016/0016-7185(71)90086-8).
- Dahl-Jensen D** and 132 others (2013) Eemian interglacial reconstructed from a Greenland folded ice core. *Nature* **493**, 489–494.
- Durand G and 10 others** (2006) Effect of impurities on grain growth in cold ice sheets. *Geophysical Research: Earth Surface* **111**(F01015), 1–18. doi: [10.1029/2005JF000320](https://doi.org/10.1029/2005JF000320).
- Duval P, Ashby MF and Anderman I** (1983) Rate-controlling processes in the creep of polycrystalline ice. *The Journal of Physical Chemistry* **87**(21), 4066–4074. doi: [10.1021/j100244a014](https://doi.org/10.1021/j100244a014).
- Fastook JL, Head JW and Marchant DR** (2014) Formation of lobate debris aprons on Mars: assessment of regional ice sheet collapse and debris-cover armoring. *Icarus* **228**, 54–63. doi: [10.1016/j.icarus.2013.09.025](https://doi.org/10.1016/j.icarus.2013.09.025)
- Feldman WC** (2004) Gamma-ray, neutron, and alpha-particle spectrometers for the Lunar Prospector mission. *Journal of Geophysical Research* **109**(E7), E07S06. doi: [10.1029/2003JE002207](https://doi.org/10.1029/2003JE002207).
- Forget F, Haberle RM, Montmessin F, Levrard B and Head JW** (2006) Formation of glaciers on Mars by atmospheric precipitation at high obliquity. *Science* **311**(5759), 368–371. doi: [10.1126/science.1120335](https://doi.org/10.1126/science.1120335).
- Gardner C** (1992) Ranging performance of satellite laser altimeters. *IEEE Transactions on Geoscience and Remote Sensing* **30**(5), 1061–1072. doi: [10.1109/36.175341](https://doi.org/10.1109/36.175341).
- Garvin JB, Head JW, Marchant DR and Kreslavsky MA** (2006) High-latitude cold-based glacial deposits on Mars: multiple superposed drop moraines in a crater interior at 70N latitude. *Meteoritics & Planetary Science* **41**(10), 1659–1674. doi: [10.1111/j.1945-5100.2006.tb00443.x](https://doi.org/10.1111/j.1945-5100.2006.tb00443.x).
- Gillet-Chaulet F, Hindmarsh RCA, Corr HFJ, King EC and Jenkins A** (2011) In-situ quantification of ice rheology and direct measurement of the Raymond Effect at Summit, Greenland using a phase-sensitive radar. *Geophysical Research Letters* **38**(L24503), 1–6. doi: [10.1029/2011GL049843](https://doi.org/10.1029/2011GL049843).
- Glen JW** (1955) The creep of polycrystalline ice. *Proc. Royal Soc. Lond.* **228**(1175), 519–538. doi: [10.1098/rspa.1955.0066](https://doi.org/10.1098/rspa.1955.0066).
- Goldsby DL and Kohlstedt DL** (2001) Superplastic deformation of ice: experimental observations. *Journal of Geophysical Research* **106**(B6), 11017–11030. doi: [10.1029/2000JB900336](https://doi.org/10.1029/2000JB900336).
- Grima C and 7 others** (2009) North polar deposits of Mars: extreme purity of the water ice. *Geophysical Research Letters* **36**(3), n/a–n/a. doi: [10.1029/2008GL036326](https://doi.org/10.1029/2008GL036326).
- Grimm RE, Harrison KP, Stillman DE and Kirchoff MR** (2017) On the secular retention of ground water and ice on Mars. *Journal of Geophysical Research Planets* **122**(1), 94–109. doi: [10.1002/2016JE005132](https://doi.org/10.1002/2016JE005132).
- Gwinner K and 9 others** (2010) Topography of Mars from global mapping by HRSC high-resolution digital terrain models and orthoimages: characteristics and performance. *Earth and Planetary Science Letters* **294**(3–4), 506–519. doi: [10.1016/j.epsl.2009.11.007](https://doi.org/10.1016/j.epsl.2009.11.007).
- Head JW, Mustard JF, Kreslavsky Ma, Milliken RE and Marchant DR** (2003) Recent ice ages on Mars. *Nature* **426**(6968), 797–802. doi: [10.1038/nature02114](https://doi.org/10.1038/nature02114).
- Head JW, Marchant DR, Dickson JL, Kress AM and Baker DM** (2010) Northern mid-latitude glaciation in the Late Amazonian period of Mars: criteria for the recognition of debris-covered glacier and valley glacier land-system deposits. *Earth and Planetary Science Letters* **294**(3–4), 306–320. doi: [10.1016/j.epsl.2009.06.041](https://doi.org/10.1016/j.epsl.2009.06.041).
- Holt JW and 11 others** (2008) Radar sounding evidence for buried glaciers in the southern mid-latitudes of Mars. *Science* **322**(5905), 1235–1238. doi: [10.1126/science.1164246](https://doi.org/10.1126/science.1164246).
- Hubbard B, Souness C and Brough S** (2014) Glacier-like forms on Mars. *Cryosphere* **8**(6), 2047–2061. doi: [10.5194/tc-8-2047-2014](https://doi.org/10.5194/tc-8-2047-2014).
- Karlsson NB, Holt JW and Hindmarsh RCA** (2011) Testing for flow in the north polar layered deposits of Mars using radar stratigraphy and a simple 3D ice-flow model. *Geophysical Research Letters* **38**(24), n/a–n/a. doi: [10.1029/2011GL049630](https://doi.org/10.1029/2011GL049630).
- Karlsson NB, Schmidt LS and Hvidberg CS** (2015) Volume of Martian mid-latitude glaciers from radar observations and ice flow modeling. *Geophysical Research Letters* **42**(8), 2627–2633. doi: [10.1002/2015GL063219](https://doi.org/10.1002/2015GL063219).
- Kieffer HH** (1990) H₂O grain size and the amount of dust in Mars' residual north polar cap. *Journal of Geophysical Research* **95**(B2), 1481. doi: [10.1029/JB095iB02p01481](https://doi.org/10.1029/JB095iB02p01481).
- Kim J and Muller JP** (2009) Multi-resolution topographic data extraction from Martian stereo imagery. *Planetary and Space Science* **57**(14–15), 2095–2112. doi: [10.1016/J.PSS.2009.09.024](https://doi.org/10.1016/J.PSS.2009.09.024).
- Koutnik MR, Waddington ED and Winebrenner DP** (2009) A method to infer past surface mass balance and topography from internal layers in martian polar layered deposits. *Icarus* **204**(2), 458–470. doi: [10.1016/J.ICARUS.2009.06.019](https://doi.org/10.1016/J.ICARUS.2009.06.019).
- Laskar J, Levrard B and Mustard JF** (2002) Orbital forcing of the martian polar layered deposits. *Nature* **419**, 375–377. doi: [10.1038/nature01066](https://doi.org/10.1038/nature01066).
- Levy JS, Fassett CI, Head JW, Schwartz C and Watters JL** (2014) Sequestered glacial ice contribution to the global Martian water budget: geometric constraints on the volume of remnant, midlatitude debris-covered glaciers. *Journal of Geophysical Research E, Planets* **119**(10), 2188–2196. doi: [10.1002/2014JE004685](https://doi.org/10.1002/2014JE004685).
- Madeleine JB and 5 others** (2009) Amazonian northern mid-latitude glaciation on Mars: a proposed climate scenario. *Icarus* **203**(2), 390–405. doi: [10.1016/j.icarus.2009.04.037](https://doi.org/10.1016/j.icarus.2009.04.037).
- Mangold N** (2003) Geomorphic analysis of lobate debris aprons on Mars at Mars Orbiter Camera scale: evidence for ice sublimation initiated by fractures. *Journal of Geophysical Research* **108**(4), E8021. doi: [10.1029/2002JE001885](https://doi.org/10.1029/2002JE001885).
- Mellon MT and Jakosky BM** (1995) The distribution and behavior of Martian ground ice during past and present epochs. *Journal of Geophysical Research* **100**(E6), 11781. doi: [10.1029/95JE01027](https://doi.org/10.1029/95JE01027).
- Milliken RE, Mustard JF and Goldsby DL** (2003) Viscous flow features on the surface of Mars: observations from high-resolution Mars Orbiter Camera (MOC) images. *Journal of Geophysical Research* **108**(E6), 5057. doi: [10.1029/2002JE002005](https://doi.org/10.1029/2002JE002005).
- Miyamoto H, Mitri G, Showman AP and Dohm JM** (2005) Putative ice flows on Europa: geometric patterns and relation to topography collectively constrain material properties and effusion rates. *Icarus* **177**(2), 413–424. doi: [10.1016/J.ICARUS.2005.03.014](https://doi.org/10.1016/J.ICARUS.2005.03.014).
- Parsons R and Holt J** (2016) Constraints on the formation and properties of a Martian lobate debris apron: insights from high-resolution topography, SHARAD radar data, and a numerical ice flow model. *Journal of Geophysical Research, Planets* **121**(3), 432–453. doi: [10.1002/2015JE004927](https://doi.org/10.1002/2015JE004927).
- Paterson WSB** (1977) Secondary and tertiary creep of glacier ice as measured by borehole closure rates. *Reviews of Geophysics (Washington, D.C.)* **15**(1), 47. doi: [10.1029/RG015i001p00047](https://doi.org/10.1029/RG015i001p00047).
- Pathare AV and Paige DA** (2005) The effects of martian orbital variations upon the sublimation and relaxation of north polar troughs and scarps. *Icarus* **174**(2), 419–443. doi: [10.1016/J.ICARUS.2004.10.030](https://doi.org/10.1016/J.ICARUS.2004.10.030).
- Pathare AV, Paige DA and Turtle E** (2005) Viscous relaxation of craters within the martian south polar layered deposits. *Icarus* **174**(2), 396–418. doi: [10.1016/J.ICARUS.2004.10.031](https://doi.org/10.1016/J.ICARUS.2004.10.031).
- Peltier WR, Goldsby DL, Kohlstedt DL and Tarasov L** (2000) Ice-age ice-sheet rheology: constraints from the last glacial maximum form of the laurentide ice sheet. *Annals of Glaciology* **30**, 163–176. doi: [10.3189/172756400781820859](https://doi.org/10.3189/172756400781820859).
- Plaut JJ and 7 others** (2009) Radar evidence for ice in lobate debris aprons in the mid-northern latitudes of Mars. *Geophysical Research Letters* **36**(2), 1–4. doi: [10.1029/2008GL036379](https://doi.org/10.1029/2008GL036379).
- Qi C, Stern LA, Pathare A, Durham WB and Goldsby DL** (2018) Inhibition of grain boundary sliding in fine-grained ice by intergranular particles: implications for planetary ice masses. *Geophysical Research Letters* **45**(23), 12757–12765. doi: [10.1029/2018GL080228](https://doi.org/10.1029/2018GL080228).
- Richardson MI and Wilson RJ** (2002) Investigation of the nature and stability of the Martian seasonal water cycle with a general circulation model. *Journal of Geophysical Research* **107**(E5), 5031. doi: [10.1029/2001JE001536](https://doi.org/10.1029/2001JE001536).
- Schmidt LS** (2019) *Short-and Long-term Model Simulations of the Evolution of Vatnajökull Ice Cap* (Ph.d. thesis). University of Iceland.
- Seu R and 11 others** (2007) SHARAD sounding radar on the Mars Reconnaissance Orbiter. *Journal of Geophysical Research E, Planets* **112**(5), 1–18. doi: [10.1029/2006JE002745](https://doi.org/10.1029/2006JE002745).

- Sori MM, Byrne S, Hamilton CW and Landis ME** (2016) Viscous flow rates of icy topography on the north polar layered deposits of Mars. *Geophysical Research Letters* **43**(2), 541–549. doi: [10.1002/2015GL067298](https://doi.org/10.1002/2015GL067298).
- Sori MM and 8 others** (2017) The vanishing cryovolcanoes of Ceres. *Geophysical Research Letters* **44**(3), 1243–1250. doi: [10.1002/2016GL072319](https://doi.org/10.1002/2016GL072319).
- Souness C, Hubbard B, Milliken RE and Quincey D** (2012) An inventory and population-scale analysis of martian glacier-like forms. *Icarus* **217**(1), 243–255. doi: [10.1016/j.icarus.2011.10.020](https://doi.org/10.1016/j.icarus.2011.10.020).
- Squyres SW** (1979) The distribution of lobate debris aprons and similar flows on Mars. *Journal of Geophysical Research, Solid Earth* **84**(B14), 8087–8096. doi: [10.1029/JB084iB14p08087](https://doi.org/10.1029/JB084iB14p08087).
- Viola D, McEwen A, Dundas C and Byrne S** (2015) Expanded secondary craters in the Arcadia Planitia region, Mars: evidence for tens of Myr-old shallow subsurface ice. *Icarus* **248**, 190–204. doi: [10.1016/j.icarus.2014.10.032](https://doi.org/10.1016/j.icarus.2014.10.032).
- Weertman J** (1983) Creep deformation of ice. *Annual Review of Earth and Planetary Sciences* **11**, 215–240.
- Weitz N, Zanetti M, Osinski G and Fastook J** (2018) Modeling concentric crater fill in Utopia Planitia, Mars, with an ice flow line model. *Icarus* **308**, 209–220. doi: [10.1016/J.ICARUS.2017.08.023](https://doi.org/10.1016/J.ICARUS.2017.08.023).
- Winebrenner DP and 6 others** (2008) Evidence for ice flow prior to trough formation in the martian north polar layered deposits. *Icarus* **195**(1), 90–105. doi: [10.1016/J.ICARUS.2007.11.030](https://doi.org/10.1016/J.ICARUS.2007.11.030).